UC Davis
UC Davis Previously Published Works

Title

Copper migration and surface oxidation of CuxBi2Se3 in ambient pressure environments

Permalink

Journal

ISSN

Authors

Gross, Adam L
Falling, Lorenz
Staab, Matthew C
et al.

Publication Date

DOI

Copyright Information

Peer reviewed

Copper migration and surface oxidation of $Cu_xBi_2Se_3$ in ambient pressure environments

To cite this article: Adam L Gross *et al* 2022 *J. Phys. Mater.* **5** 044005

View the article online for updates and enhancements.

Journal of Physics: Materials

Copper migration and surface oxidation of Cu$_x$Bi$_2$Se$_3$ in ambient pressure environments

Adam L Gross[1] , Lorenz Falling[2] , Matthew C Staab[1] , Metzli I Montero[1], Rahim R Ullah[1],
David M Nisson[1], Peter Klavins[1], Kristie J Koski[3] , Nicholas J Curro[1] , Valentin Taufour[1] ,
Slavomir Nemsak[1,2] and Inna M Vishik[1,*]

1   Department of Physics and Astronomy, University of California, Davis, CA 95616, United States of America
2   Advanced Light Source, Lawrence Berkeley National Lab, Berkeley, CA 94720, United States of America
3   Department of Chemistry, University of California, Davis, CA 95616, United States of America
*   Author to whom any correspondence should be addressed.

E-mail: ivishik@ucdavis.edu

Abstract

Chemical modifications such as intercalation can be used to modify surface properties or to further
functionalize the surface states of topological insulators (TIs). Using ambient pressure x-ray
photoelectron spectroscopy, we report copper migration in Cu$_x$Bi$_2$Se$_3$, which occurs on a timescale
of hours to days after initial surface cleaving. The increase in near-surface copper proceeds along
with the oxidation of the sample surface and large changes in the selenium content. These complex
changes are further modeled with core-level spectroscopy simulations, which suggest a
composition gradient near the surface which develops with oxygen exposure. Our results shed light
on a new phenomenon that must be considered for intercalated TIs—and intercalated materials in
general—that surface chemical composition can change when specimens are exposed to ambient
conditions.

1. Introduction

Topological insulators (TIs) have attracted significant interest from the quantum materials community for
their surface electronic structures, notably surface Dirac fermions with spin-momentum locking that are
robust to disorder and defects [1–4]. Chemical intercalation of TIs (i.e. the insertion of atoms or molecules
between quintuple layers) can further modify the material properties [5–12] or create additional electronic
phenomena, such as superconductivity with Cu intercalation that has a maximum superconducting critical
temperature of $T_{c,\max} \approx 3.8\,\text{K}$ [10, 13–19]. The Cu-intercalated TI Bi$_2$Se$_3$ (Cu$_x$Bi$_2$Se$_3$) is a known
superconductor, with $T_{c,\max}$ and the superconducting shielding fraction strongly depending on the Cu
content and preparation method [14–16, 20]. Controlling the Cu content and its variation during and after
synthesis is thus important for realizing ideal superconducting properties in Cu$_x$Bi$_2$Se$_3$.

Intercalated materials may be exposed to air during sample preparation or real world usage, such as in
the operation of devices, which may affect composition. For instance, the intercalate guest can diffuse within
battery cells left at a fixed potential, and it is known that intercalants can diffuse within and between layers in
various compounds [12, 21–23]. The effect of ambient conditions on intercalant chemistry is not fully
understood due to experimental difficulties, despite its practical importance.

In this work, we use Cu$_x$Bi$_2$Se$_3$ as a representative material to establish the effects of controlled ambient
environments on evolving chemistry in the near-surface region in intercalated TIs. Using x-ray photoelectron
spectroscopy (XPS), the near-surface Cu composition was found to increase under both controlled O$_2$ dosing
and ambient air exposure, coincident with the formation and growth of an oxide layer that is strongest in full
atmosphere. Lastly, core-electron spectroscopy simulations show that our XPS observations are consistent
with a sample developing vertical gradient distributions of Cu and Se upon exposure to a controlled O$_2$
environment.

2. Materials and methods

Synchrotron ambient pressure X-ray photoelectron spectroscopy (AP-XPS) experiments were performed at the Advanced Light Source Beamline 9.3.2 in a photon energy range of $E_{ph} = 230$–900 eV, with an X-ray spot size of $d \sim 1\,\text{mm}^2$. The core level spectra were collected with a Scienta R4000 HiPP electron analyzer with differential pumping, allowing the sample to remain at near-ambient pressures during data acquisition [24]. The analysis environment was initially at high vacuum ($\sim 1 \times 10^{-7}$ mbar), and then with O_2 at near-ambient pressure (0.133 mbar). The measured partial pressure of O_2 is equivalent to the total ambient pressure in the AP-XPS experiment. Longer timescale experiments were performed using a Kratos AXIS Supra$^+$ with a monochromated, unpolarized $E_{ph} = 1486.6$ eV Al-Kα source. Samples were cleaved *in situ* with the top post method in the AP-XPS experiment, and cleaved *ex situ* with Scotch tape in the Kratos XPS experiment, keeping air exposure under several minutes prior to the initial measurements. Angle-resolved photoemission spectroscopy (ARPES) spectra were collected at the Advanced Light Source Beamline 4.0.3 (MERLIN) with $E_{ph} = 39.2$ eV. Core level peaks were identified using binding energy reference values [25].

Bi$_2$Se$_3$ samples were grown using the Bridgman method, and were then intercalated with Cu to form Cu$_x$Bi$_2$Se$_3$ crystals using a solution-based process [26]. Due to the variation of Cu and Se content highlighted in our study, our convention is to use the nominal bulk stoichiometries after synthesis (Cu$_{0.15}$Bi$_2$Se$_3$ and Cu$_{0.3}$Bi$_2$Se$_3$) to distinguish between samples in our analysis. No indications of superconductivity were found in these samples, which depends on the details of the synthesis and the intercalation [20, 27] (see supplemental material for further details).

3. Results

Figure 1 provides initial XPS and ARPES characterizations of Cu$_{0.15}$Bi$_2$Se$_3$ and Cu$_{0.3}$Bi$_2$Se$_3$ at several different photon energies. Figure 1(a) shows a survey spectrum of the core levels accessible with $E_{ph} = 650$ eV in the AP-XPS experiment. The survey confirms the quality of the *in situ* cleaved sample, showing peaks for Cu, Bi, and Se. Figure 1(b) shows an ARPES spectrum from an *in situ* cleaved sample, clearly showing the topological surface state and Dirac point at $E_B \sim 0.3$ eV, demonstrating the maintenance of crystallinity and topological electronic features after Cu intercalation. Figure 1(c) shows the three core levels present in the shallow binding energy region in figure 1(a): Cu 3p, Se 3d, and Bi 5d, none of which show initial oxidation or hydroxylation. This set of three shallow core levels is sufficient to determine the chemical composition of Cu$_{0.15}$Bi$_2$Se$_3$ and Cu$_{0.3}$Bi$_2$Se$_3$ throughout the oxidation process; the relative peak intensities are proportional to the elemental composition after correcting for the relative sensitivity factor (RSF) for each photon energy [28, 29]. To quantify the Cu content, we monitor the binding energy region around $E_B \sim 76$ eV where the Cu 3p doublet is present. All Cu 3p data are measured above the loss feature-containing background (figures 1(d) and (e)).

To accurately quantify the Cu content in figure 1, which is present on top of a relatively large background, we utilize a background correction procedure incorporating the electron energy loss features in the Cu$_{0.3}$Bi$_2$Se$_3$ XPS spectrum. The loss features near $E_B \sim 72$ eV (green and cyan curves in figures 1(d) and (e)) originate from bulk plasmon resonances in Bi$_2$Se$_3$ [30]. Since this background is also present in a Bi$_2$Se$_3$ reference sample from the same batch (figure 1(d)), we use the Bi$_2$Se$_3$ spectrum from a newly cleaved sample as a reference for fitting to the plasmon losses in the Cu$_{0.3}$Bi$_2$Se$_3$ spectrum (figure 1(e)). After fitting Voigt peaks to the Se 3d peaks and the loss features in the reference spectrum, the result is a background containing the loss features in the vicinity of the Cu 3p doublet (dashed curve). Fitting this background to the Cu$_{0.3}$Bi$_2$Se$_3$ spectrum allows us to isolate the Cu 3p signal intensity, shown as a separate Voigt doublet (brown curve). The areas of the fitted Cu, Se, and Bi peaks then correspond to the total XPS intensity for these elements. Additional information on the Cu quantification, RSF assumptions, and plasmon loss feature correction can be found in the supplemental material.

Figure 2 shows the main results of the AP-XPS experiment, which track the evolution of the Cu and Se composition from an initial condition with no O_2 dosingand later times in 0.133 mbar O_2 to simulate ambient atmosphere. The chemical compositions are expressed in terms of the atomic ratios of Cu/Bi and Se/Bi for each time and photon energy, with the Cu fraction $x = 2 \times$ Cu/Bi. To determine the atomic ratios, the XPS intensities determined from the peak fitting were weighed by the RSF for each element and photon energy (see supplemental material). The atomic ratios are normalized to Bi since Bi changes relatively less compared to Cu and Se in our experiments.

Over the course of the four day experiment, the Cu fraction x increases from $x = 0.13$ to $x = 0.40$ after dosing O_2 for the $E_{ph} = 900$ eV data, with smaller changes seen at lower, more surface sensitive E_{ph} (figure 2(a)). The growth of the Cu/Bi ratio is consistent with Cu migrating vertically to the probed-surface region of the sample, since the only additional Cu present is deeper within the sample, with no external Cu
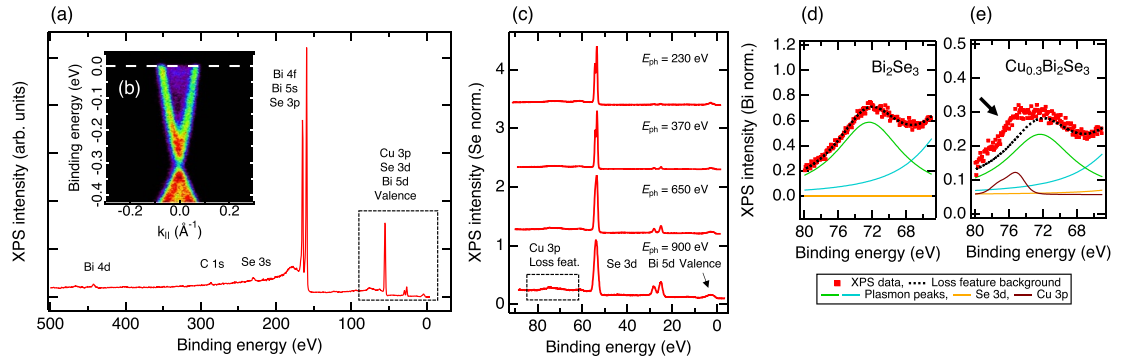
Figure 1. XPS and ARPES characterizations of freshly cleaved $Cu_{0.15}Bi_2Se_3$ and $Cu_{0.3}Bi_2Se_3$. (a) $Cu_{0.15}Bi_2Se_3$ survey spectrum taken with $E_{ph} = 650\,eV$ in vacuum. Cu, Bi, and Se core levels are labeled, with the dashed box indicating the shallow core levels analyzed in this work. The adventitious C 1s peak is also labeled. (b) ARPES spectrum of the topological surface state in $Cu_{0.15}Bi_2Se_3$. (c) $Cu_{0.15}Bi_2Se_3$ shallow core levels in the dashed box taken with $E_{ph} = 230\,eV$, $370\,eV$, $650\,eV$, and $900\,eV$ in vacuum. For best comparison, spectra are shown normalized to their Se 3d peaks and offset for clarity. (d) Illustration of the loss feature background in a Bi_2Se_3 sample, with the individual plasmon resonances indicated in green and cyan. (e) Corresponding spectrum in $Cu_{0.3}Bi_2Se_3$ showing the Cu 3p peaks (brown curve) and loss feature background after dosing 0.133 mbar O_2. The black arrow indicates the additional spectral weight from the Cu. Figures (d) and (e) were taken with $E_{ph} = 370\,eV$.
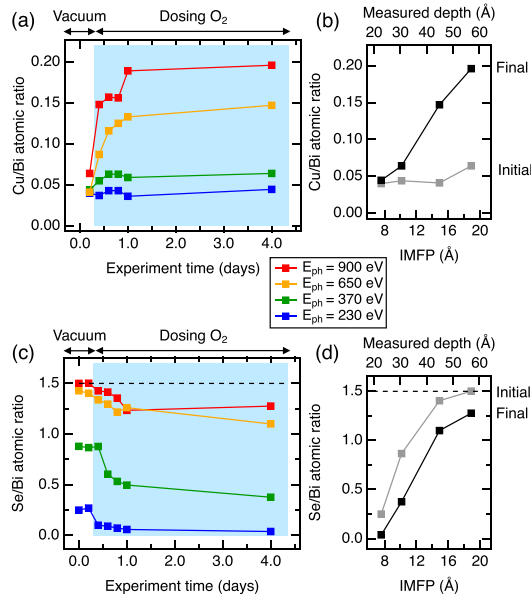

Figure 2. Evolution of Cu and Se composition in $Cu_{0.3}Bi_2Se_3$ in the AP-XPS experiment. (a) Cu/Bi atomic ratios for four different photon energies, initially in vacuum and after in 0.133 mbar O_2. (b) Initial and final Cu/Bi ratios plotted versus the IMFP and the measured depth ($3 \times$ IMFP) for each E_{ph} in (a). Initial: in vacuum after cleaving; final: in 0.133 mbar O_2 for four days. (c) Se/Bi atomic ratios for the same photon energies and conditions. Dashed line at Se/Bi = 1.5 indicates the ideal Se/Bi = $3/2$ ratio. (d) Initial and final Se/Bi atomic ratios from (c) plotted versus IMFP and measured depth.

deposition. This is best seen when plotted versus the inelastic mean free path (IMFP) for each photon energy in figure 2(b), which provides a length scale for the observed Cu migration. The measured depth ($3 \times$ IMFP) at each photon energy includes depths below one IMFP, which still contribute to the XPS measurement. A similar plot of the Se/Bi ratio is shown in figure 2(c), showing a steady decrease in Se/Bi at all E_{ph} after dosing O_2, decreasing from the ideal Se/Bi = $3/2$ ratio of Bi_2Se_3. There are large differences in the initial and final Se/Bi ratios for the different E_{ph}, implying a large variation in the Se distribution, with the bulk being rich in Se and the surface being deficient in Se (figure 2(d)). Between one and four days in the AP-XPS chamber, the changes to Cu/Bi and Se/Bi are less pronounced than those that happen immediately after dosing O_2. Similar trends have also been observed in another AP-XPS experiment in a mixed O_2/H_2O environment (see supplemental material).

Figure 3 shows the initial and final Bi 5d peaks for all E_{ph} before and after dosing O_2, quantifying the growth of bismuth oxide. The initial state peaks are well separated, showing little to no signs of Bi oxidation (figure 3(a)). After four days in the AP-XPS chamber, chemically-shifted peaks are present for
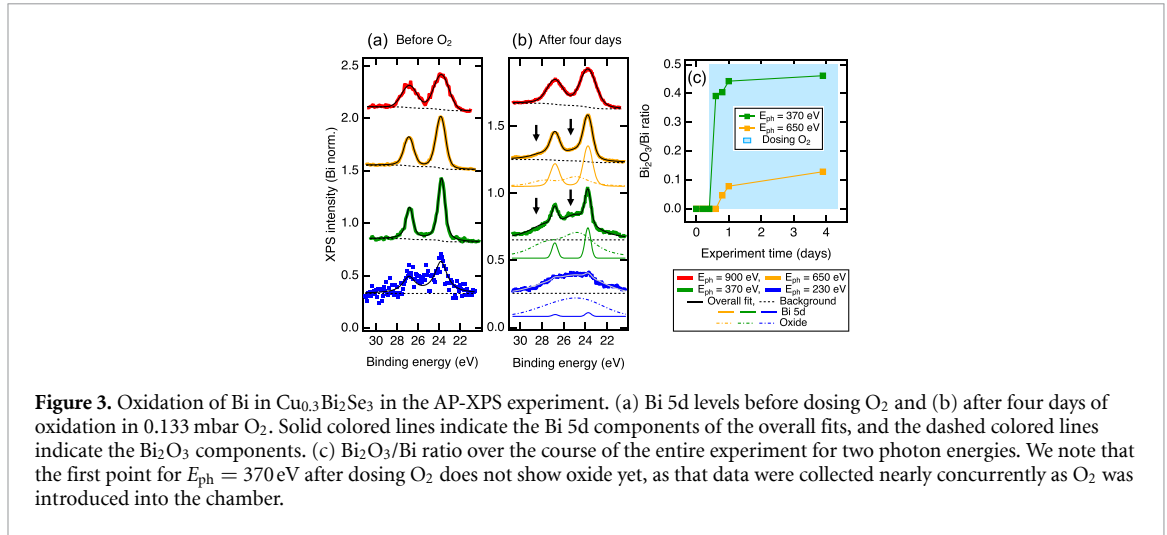
Figure 3. Oxidation of Bi in $Cu_{0.3}Bi_2Se_3$ in the AP-XPS experiment. (a) Bi 5d levels before dosing O_2 and (b) after four days of oxidation in 0.133 mbar O_2. Solid colored lines indicate the Bi 5d components of the overall fits, and the dashed colored lines indicate the Bi_2O_3 components. (c) Bi_2O_3/Bi ratio over the course of the entire experiment for two photon energies. We note that the first point for $E_{ph} = 370$ eV after dosing O_2 does not show oxide yet, as that data were collected nearly concurrently as O_2 was introduced into the chamber.
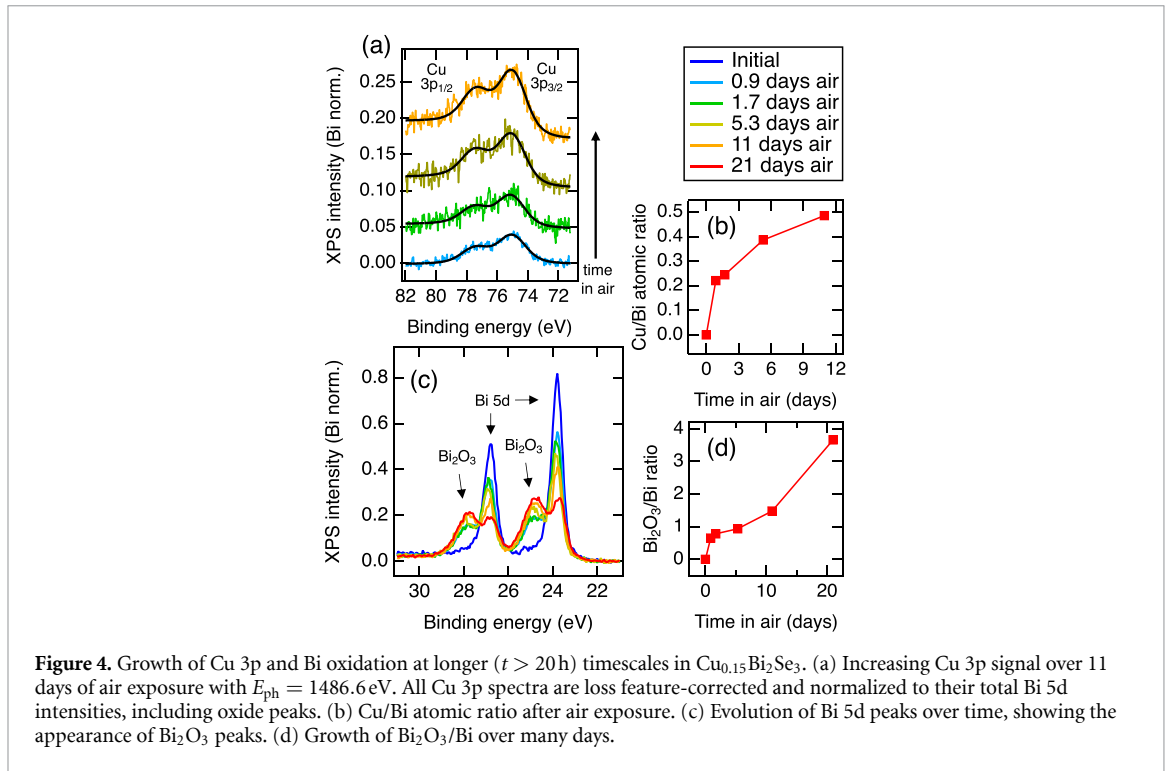

Figure 4. Growth of Cu 3p and Bi oxidation at longer ($t > 20$ h) timescales in $Cu_{0.15}Bi_2Se_3$. (a) Increasing Cu 3p signal over 11 days of air exposure with $E_{ph} = 1486.6$ eV. All Cu 3p spectra are loss feature-corrected and normalized to their total Bi 5d intensities, including oxide peaks. (b) Cu/Bi atomic ratio after air exposure. (c) Evolution of Bi 5d peaks over time, showing the appearance of Bi_2O_3 peaks. (d) Growth of Bi_2O_3/Bi over many days.

$E_{ph} = 650$ eV, 370 eV, and 230 eV (figure 3(b), dashed colored lines). These changes to the Bi levels directly show the formation of Bi_2O_3 at the surface, which is most dominant at lower E_{ph}. The noise in the initial $E_{ph} = 230$ eV spectrum (blue, left) is due to the low photon flux at this particular E_{ph}, which was improved for the final state (blue, right) by extending the measurement time. The large width of the oxide components in the Bi 5d spectra suggest a convolution of several electrostatically distinct (i.e. band bent) or chemically distinctive states, which are most pronounced in the spectrum measured with highest surface sensitivity ($E_{ph} = 230$ eV). Figure 3(c) quantifies the growth of the Bi_2O_3 peaks relative to the total Bi peak intensity, showing that oxidation starts after dosing O_2, with a larger oxide fraction seen with the more surface-sensitive $E_{ph} = 370$ eV. When compared to the $E_{ph} = 650$ eV data, the overall detected oxide is less and with a more gradual onset due to the lower surface sensitivity of $E_{ph} = 650$ eV. Interestingly, most of the oxidation process occurs within the first day and only little change is observed thereafter, as is the case with the Cu and Se changes.

To gain insight into changes in the $Cu_{0.15}Bi_2Se_3$ composition over longer timescales ($t > 20$ h), we continue by performing a different set of lab-based XPS measurements on an *exsitu* cleaved $Cu_{0.15}Bi_2Se_3$ sample after air exposure in full atmosphere, with increasing periods of air exposure. The loss feature-corrected spectra for Cu 3p are shown in figure 4(a), showing large changes in the Cu/Bi atomic ratio

after air exposure for multiple days (figure 4(b)). In figure 4(c), we again see the oxidation of the surface, with the Bi oxide strongly growing over several weeks. The evolution of Bi_2O_3 in figure 4(d) shows an initial jump after exposure to air for 0.9 days, and continues to grow afterward. Oxidation of Se is also seen (see supplemental material), and we note that this sample had a smaller initial Cu concentration than the sample measured with AP-XPS.

4. Discussion

Our interpretation of the present data is guided by prior studies of pristine Bi_2Se_3 exposed to air and controlled ambient environments. The effects of ambient conditions on regular Bi_2Se_3 have been studied in the following ways with the following conclusions. Exposure to ambient environments has been shown to alter measured ARPES spectra and the surface composition in Bi_2Se_3 [31–34]. The topological surfaces states can be modified by forming 2D quantum well states in ambient conditions [32], and can present band-bending and controlled charge-doping after dosing H_2O [31] and UV irradiation [35]. In most cases, the robust topological surface states are still present in Bi_2Se_3 despite air exposure and oxidation [32, 36]. The thinness of the oxide layer and the robustness of the topological surface states are common themes in Bi_2Se_3, including the persistence of surface states in intercalated samples [23, 37], with some works not reporting any surface reactivity [38, 39]. Still, the surface chemistry in Bi_2Se_3 remains an open question, particularly after intercalation.

To begin the discussion of our results, we first turn to the observations seen in the AP-XPS experiment. The main result in figure 2 shows that the increase in the Cu 3p peak intensity over the course of the experiment is coincident with the introduction of O_2 gas, showing that Cu migrates to the surface region during measurement. This behavior has not been previously reported or quantified in a TI with XPS, although some indications of Cu near the surface have been reported with scanning tunneling microscopy imaging after cleaving [14].

The probing depth in XPS is mainly limited by the IMFP of escaped electrons at each E_{ph}, so measurement with several different E_{ph} to vary IMFP allows one to obtain a depth profile of the elements in the sample. In the $E_{ph} = 230$–900 eV photon energy range in $Cu_{0.3}Bi_2Se_3$, the IMFP of Cu 3p photoelectrons increases from 7.6 to 18.9 Å, calculated in QUASES using the TPP2M algorithm [40].

Measured XPS intensities generally follow an exponential form for attenuation [41]:

$$dI = I_0 \cdot X(z) \cdot e^{-z/\lambda \cos(\theta)} dz, \tag{1}$$

with a total emitted photoelectron intensity I_0, vertical depth z, atomic fraction $X(z)$ at each depth z, the IMFP λ, and the photoelectron collection angle θ from the surface normal. From equation (1), the measured photoelectron intensity is $I \approx 0.95I_0$ within three IMFPs below the surface, providing an upper limit for the probing depth. Figure 2(b) shows the initial and final distributions of Cu/Bi as a function of IMFP and the measured depth (3λ) in the AP-XPS experiment (black and gray solid lines), showing the growth of Cu from deeper within the sample. The greatest Cu increase is at an IMFP of 18.9 Å, which corresponds to Cu migrating into the top 6 nm surface region of the sample.

We note that the observed Cu migration is very small when measured with $E_{ph} = 230$ eV, which indicates that the topmost layer of the sample is dominated by the surface bismuth oxide. The beamline photon flux is also considerably lower at $E_{ph} = 230$ eV, which can contribute to measurement error.

Another notable observation is the decrease in Se content relative to Bi in figure 2(c) over the course of the AP-XPS experiment. Initially after cleaving (that is, prior to the first data points in figure 2(c)), the Se 3d intensity is already reduced, which continues to drop over the course of the experiment from the ideal $Se/Bi = 3/2$. The initial distribution of Se when expressed versus IMFP in figure 2(d) shows that the uppermost 2 nm (two quintuple layers) is deficient in Se, while the uppermost 6 nm (six quintuple layers) is richer in Se and representative of bulk stoichiometric Bi_2Se_3. After four days in O_2, Se/Bi decreases at all depths.

The observation of a long Se gradient with minimal Se at the surface is consistent with the well known volatility of Se in Bi_2Se_3. Bi_2Se_3 generally has selenium vacancies which make samples naturally *n*-type without further chemical compensation [31, 32, 42–48]. However, our results indicate that these selenium vacancies may be more concentrated near the surface, and the deeper bulk is closer to nominal stoichiometry. The pure Bi_2Se_3 reference sample also shows a decrease in Se after dosing O_2, and with the decrease more significant at the surface. See the supplemental material for a comparison to the Se/Bi ratio in Bi_2Se_3. The Fermi level E_F in the ARPES spectrum in figure 1(b) intersects the bulk conduction band, confirming that this specimen is *n*-type at the surface region, with an IMFP of 4.9 Å for $E_{ph} = 39.2$ eV calculated in QUASES. Cu doping is also known to shift the chemical potential further into the bulk conduction band [46].

A prior XPS/atomic force microscopy study has observed small Bi islands that appear within 1 h after cleaving [33], which is also consistent with decreasing Se/Bi in figure 2(c), suggesting that some Bi migration could also be occurring along with Cu. However, the larger increases in Cu/Bi we see suggest that any Bi migration would be very small, below the sensitivity of a standard XPS instrument [33] and indistinguishable from Bi oxide at the surface.

While Cu migration can be observed on shorter timescales, the process continues and is more easily seen at the longer timescales ($t > 25$ h) in figure 4(a). On these timescales the oxidation of the near-surface Bi is evident with new oxide peaks, consistent with prior work [33, 44] and the oxide peaks we see during the AP-XPS experiment in figure 3. The oxidation is stronger and continues for longer in full atmosphere ($P = 1013.25$ mbar) than in the AP-XPS experiment, even when considering the deeper probing depth of the $E_{ph} = 1486.6$ eV Al-Kα source (IMFP = 28.9 Å). The oxidation is accompanied by a steady increase in Cu 3p over several days (figure 4(b)), greater than what was observed in AP-XPS. The link between oxidation and Cu migration is clear when looking at the trends in figures 2–4: both Cu migration and Bi_2O_3 formation start right after dosing O_2, and when oxide growth slows between one and four days, Cu growth also slows, changing only slightly. This suggests that surface oxides establish the conditions needed for Cu to diffuse towards the surface. Our observations in figure 4 suggest that surface oxidation and Cu migration continues slowly for months in air, until the oxidation becomes self-limiting.

There are several microscopic mechanisms that can promote Cu migration, such as a surface work function mismatch between Bi_2O_3 and $Cu_xBi_2Se_3$ that can drive the Cu to the surface with a built-in E-field. The work function difference between Bi_2O_3 and Bi_2Se_3 is estimated to be ∼1.6 eV [49, 50], which would create a sufficiently large E-field near the surface. Cu is able to occupy five different sites in the van der Waals gap and in interstitial vacancies [45, 46], and some migration could be driven by Cu diffusion among these sites. Occupation of surface Se vacancies by Cu could also influence the Cu migration to the surface, which is possible due to the amphoteric character of Cu impurities in Bi_2Se_3 [51]. It is likely that Cu migration can happen for different intercalation and synthesis methods, which has been previously observed in electrochemically intercalated $Cu_xBi_2Se_3$ [12], but may vary depending on the synthesis method.

To connect the proposed changes in chemical composition to the measured XPS intensities, we model our experimental results with core-electron spectroscopy simulations using the National Institute of Standards and Technology Simulation of Electron Spectra for Surface Analysis (SESSA) software/database [52, 53]. SESSA can accurately simulate XPS spectra and peak intensities for different experimental conditions, geometries, and sample compositions using database reference values. As strongly suggested by our experimental observations, Cu and Se form a compositional gradient in the near-surface region of the material. A gradient structure consisting of several discretized, homogeneous layers with varying Cu, Bi, and Se compositions models a sample with Cu and Se gradients, shown in figures 5(a) and (b). The initial Cu distribution is assumed to be constant. The gradients have a $X(Z) = Ae^{-Z/L} + B$ falloff when approaching the surface, with fitting parameters A, L, and B chosen to match the boundary conditions observed in experiment. Due to the oxidation present after O_2 dosing, the final simulated structure is capped with a thin 2 Å overlayer of Bi_2O_3. Modeling the topmost 10 Å of $Cu_xBi_2Se_y$ is motivated by the fact that the topmost 10 Å contributes predominately to the measured XPS intensities, as it is on the order of one IMFP. Below the topmost 10 Å, we model the Cu and Se distributions as constant, equal to the maximum of the gradient. Additionally, 10 Å is the approximate thickness of one quintuple layer in Bi_2Se_3, and the van der Waals gap can temporarily serve as a barrier to deeper oxidation of the material [33]. Thus, it is likely that the oxidation is limited to the uppermost quintuple layer in the AP-XPS experiment, with lesser contributions below.

The red points in figures 5(c) and (d) show the SESSA-calculated peak intensities for the initial and final structures, expressed in terms of the Cu/Bi and Se/Bi intensity ratios versus IMFP and the measurement depth. The SESSA-calculated intensity ratios are compared to the experimental XPS intensity ratios to confirm agreement between the model and the experimental data. In the initial state, a structure with a single homogeneous Cu composition with no Cu gradient matches closely with the observed constant dependence versus IMFP in figure 2(b). Initially, no Cu has migrated into the surface regions and no oxide has formed yet. In the final state after oxidation, the dual Cu, Se gradient structure agrees best with our measured XPS intensities in figures 5(c) and (d), capturing both the increase in Cu and decrease in Se near the surface. We note that there is greater error when comparing the gradient to experiment at the smallest depth, due to the low photon flux at $E_{ph} = 230$ eV.

There are other factors that are not present in this model which can also affect the evolution of $Cu_xBi_2Se_3$ surface chemistry. These include imperfect cleaves that can form step edge sites for oxidation [34], lingering Cu remaining at the surface after the cleave, different Bi, Se surface terminations [42], as well as nanosheet morphology [44, 54]. Other Cu, Se compositional distributions are possible and consistent with our experimental observations, such as ones with discontinuous step edges or sigmoidal distributions. Because of the exponential photoelectron falloff at greater depths, compositional changes deeper in the sample are more
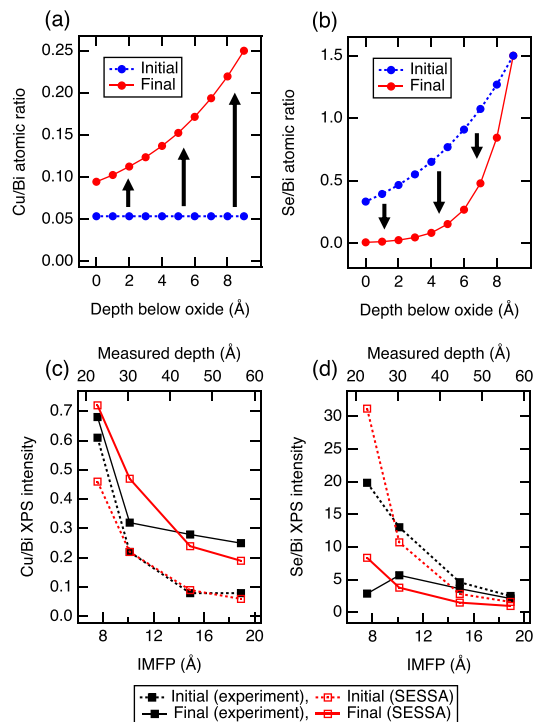
Figure 5. SESSA modeling of surface compositional gradients in $Cu_xBi_2Se_y$. (a) Proposed Cu distributions for the initial state (before dosing O_2) and the final state (after dosing O_2 for four days) at different depths below the bismuth oxide layer. The initial Cu distribution is uniform, and the final Cu distribution has developed a Cu gradient with a 2 Å thick Bi_2O_3 overlayer. The black arrows are guides to the eye indicating the passage of time. (b) Proposed Se gradients before and after dosing O_2. The final Se distribution has a steeper gradient when nearing the surface, with a 2 Å Bi_2O_3 overlayer. (c) Comparison of the AP-XPS Cu/Bi intensity ratios (black squares) to SESSA simulated intensity ratios (red squares) for the initial and final states. (d) Comparison of the AP-XPS Se/Bi intensity ratios (black squares) to SESSA simulated intensity ratios.

difficult to detect. Thus there may also be less significant compositional changes occurring below the topmost 10 Å, but still within the overall measurement depth, which our model does not include.

5. Conclusion

In summary, we have observed an increase in the surface Cu content in the intercalated TI $Cu_xBi_2Se_3$ with AP-XPS measurements. Our results show that Cu migrates to the surface and is enhanced by the appearance and growth of a bismuth surface oxide over several days, with the most pronounced changes seen in full atmosphere. Modeling Cu migration concomitant with Se depletion and oxidation matches our depth-selective XPS observations for a wide range of photon energies.

These findings show that oxidation can be used as an approach for driving chemical species towards the surface of layered intercalated materials, and add additional chemical complexity that must be considered at TI surfaces exposed to ambient conditions. Chemically tailoring the surfaces of topological materials will be needed for realizing real-world environmental applications in chemical sensing, catalysis, and electronics. Most intriguingly, the proximity of the topological surface state to the observed chemical changes in $Cu_xBi_2Se_3$ points to further study of the effect of intercalants on the surface states of TIs, particularly on timescales that allow environmental changes to influence them.
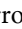
Data availability statement

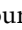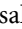The data that support the findings of this study are available upon reasonable request from the authors.

Acknowledgments

ORCID iDs

Adam L Gross ● https://orcid.org/0000-0001-9769-1183
Lorenz Falling ● https://orcid.org/0000-0002-2622-5166
Matthew C Staab ● https://orcid.org/0000-0002-3926-0104
Kristie J Koski ● https://orcid.org/0000-0002-5250-2593
Nicholas J Curro ● https://orcid.org/0000-0001-7829-0237
Valentin Taufour ● https://orcid.org/0000-0002-0024-9960
Slavomir Nemsak ● https://orcid.org/0000-0002-6103-2925
Inna M Vishik ● https://orcid.org/0000-0002-8534-9329

References

[1] Ando Y 2013 *J. Phys. Soc. Japan* **82** 102001
[2] Hasan M Z and Kane C L 2010 *Rev. Mod. Phys.* **82** 3045
[3] Wehling T, Black-Schaffer A and Balatsky A 2014 *Adv. Phys.* **63** 1
[4] Keimer B and Moore J E 2017 *Nat. Phys.* **13** 1045
[5] Paraskevopoulos K, Hatzikraniotis E, Chrisafis K, Zamani M, Stoemenos J, Economou N, Alexiadis K and Balkanski M 1988 *Mater. Sci. Eng. B* **1** 147
[6] Bludská J, Jakubec I, Karamazov S, Horák J and Uher C 2010 *J. Solid State Chem.* **183** 2813
[7] Choi Y H, Jo N H, Lee K J, Yoon J B, You C Y and Jung M H 2011 *J. Appl. Phys.* **109** 07E312
[8] Shruti V K M, Neha P, Srivastava P and Patnaik S 2015 *Phys. Rev.* B **92** 020506
[9] Mazumder K, Sharma A, Kumar Y and Shirage P M 2018 *Phys. Chem. Chem. Phys.* **20** 28257
[10] Yonezawa S 2018 *Condens. Matter* **4** 2
[11] Wang S-H, Shen D, Yang T-W, Chen I-N, Wang C-H and Wang L-M 2020 *J. Alloys Compd.* **844** 156153
[12] Kawai T, Wang C G, Kandori Y, Honoki Y, Matano K, Kambe T and Zheng GQ 2020 *Nat. Commun.* **11** 235
[13] Wray L A, Xu S-Y, Xia Y, Hor Y S, Qian D, Fedorov A V, Lin H, Bansil A, Cava R J and Hasan M Z 2010 *Nat. Phys.* **6** 855
[14] Hor Y S, Williams A J, Checkelsky J G, Roushan P, Seo J, Xu Q, Zandbergen H W, Yazdani A, Ong N P and Cava R J 2010 *Phys. Rev. Lett.* **104** 057001
[15] Sasaki S, Kriener M, Segawa K, Yada K, Tanaka Y, Sato M and Ando Y 2011 *Phys. Rev. Lett.* **107** 217001
[16] Kriener M, Segawa K, Ren Z, Sasaki S, Wada S, Kuwabata S and Ando Y 2011 *Phys. Rev.* B **84** 054513
[17] Das T, Bhattacharyya S, Joshi B P, Thamizhavel A and Ramakrishnan S 2013 *Mater. Lett.* **93** 370
[18] Matano K, Kriener M, Segawa K, Ando Y and qing Zheng G 2016 *Nat. Phys.* **12** 852
[19] Yonezawa S, Tajiri K, Nakata S, Nagai Y, Wang Z, Segawa K, Ando Y and Maeno Y 2016 *Nat. Phys.* **13** 123
[20] Schneeloch J A, Zhong R D, Xu Z J, Gu G D and Tranquada J M 2015 *Phys. Rev.* B **91** 144506
[21] Whittingham M 1978 *Prog. Solid State Chem.* **12** 41
[22] Ryabishchenkova A G, Otrokov M M, Kuznetsov V M and Chulkov E V 2015 *J. Exp. Theor. Phys.* **121** 465
[23] Ye M *et al* 2021 *J. Phys. Chem.* C **125** 1784
[24] Grass M E, Karlsson P G, Aksoy F, Lundqvist M, Wannberg B, Mun B S, Hussain Z and Liu Z 2010 *Rev. Sci. Instrum.* **81** 053106
[25] Williams G P 2001 *X-Ray Data Booklet* (Berkeley, CA: Lawrence Berkeley National Laboratory, University of California)
[26] Koski K J, Cha J J, Reed B W, Wessells C D, Kong D and Cui Y 2012 *J. Am. Chem. Soc.* **134** 7584
[27] Yu S-H, Hung T L, Ou M-N, Chou M M C and Chen Y-Y 2019 *Phys. Rev.* B **100** 174502
[28] Yeh J and Lindau I 1985 *At. Data Nucl. Data Tables* **32** 1
[29] Shard A G 2020 *J. Vac. Sci. Technol.* A **38** 041201
[30] Nascimento V, de Carvalho V, Paniago R, Soares E, Ladeira L and Pfannes H 1999 *J. Electron Spectrosc. Relat. Phenom.* **104** 99
[31] Benia H M, Lin C, Kern K and Ast C R 2011 *Phys. Rev. Lett.* **107** 177602
[32] Chen C *et al* 2012 *Proc. Natl Acad. Sci.* **109** 3694
[33] Green A J, Dey S, An Y Q, O'Brien B, O'Mullane S, Thiel B and Diebold A C 2016 *J. Vac. Sci. Technol.* A **34** 061403
[34] Thomas C R, Vallon M K, Frith M G, Sezen H, Kushwaha S K, Cava R J, Schwartz J and Bernasek S L 2015 *Chem. Mater.* **28** 35
[35] Sakamoto K *et al* 2021 *Nano Lett.* **21** 4415
[36] Yang J, Zheng B, Chen Z, Xu W, Wang R and Xu H 2020 *J. Phys. Chem.* C **124** 6253
[37] Tanaka Y *et al* 2012 *Phys. Rev.* B **85** 125111
[38] Yashina L V *et al* 2013 *ACS Nano* **7** 5181
[39] Atuchin V V *et al* 2011 *Cryst. Growth Des.* **11** 5507
[40] Tanuma S, Powell C J and Penn D R 1994 *Surf. Interface Anal.* **21** 165
[41] Tougaard S 2021 *J. Vac. Sci. Technol.* A **39** 011201
[42] Biswas D, Thakur S, Ali K, Balakrishnan G and Maiti K 2015 *Sci. Rep.* **5** 10260
[43] Bianchi M, Guan D, Bao S, Mi J, Iversen B B, King P D and Hofmann P 2010 *Nat. Commun.* **1** 128
[44] Kong D *et al* 2011 *ACS Nano* **5** 4698
[45] Tumelero M A, Faccio R and Pasa A A 2016 *J. Phys.: Condens. Matter* **28** 425801
[46] Wang Y-L *et al* 2011 *Phys. Rev.* B **84** 075335
[47] Hou Y *et al* 2019 *Nat. Commun.* **10** 5723

[48] Gross A L, Hou Y, Rossi A, Yu D and Vishik I M 2021 *Phys. Rev.* B **103** 014402
[49] Morasch J, Li S, Brötz J, Jaegermann W and Klein A 2013 *Phys. Status Solidi* a **211** 93
[50] Takane D, Souma S, Sato T, Takahashi T, Segawa K and Ando Y 2016 *Appl. Phys. Lett.* **109** 091601
[51] Vaško A, Tichý L, Horák J and Weissenstein J 1974 *Appl. Phys.* **5** 217
[52] Smekal W, Werner W S M and Powell C J 2005 *Surf. Interface Anal.* **37** 1059
[53] Werner W S M, Smekal W, and Powell C J 2017 Simulation of electron spectra for surface analysis (SESSA) version 2.1 *Technical Report*
[54] Jia G, Wu Z, Wang P, Yao J and Chang K 2016 *Sci. Rep.* **6** 22191